Article

A Practical Split-Window Algorithm for Retrieving Land Surface Temperature from Landsat-8 Data and a Case Study of an Urban Area in China

Meijun Jin [1], Junming Li [2,3,*], Caili Wang [4] and Ruilan Shang [3]

[1] College of Architecture and Civil Engineering, Taiyuan University of Technology, Yingze Street 79, Taiyuan 030024, China; E-Mail: jinmeijun@tyut.edu.cn

[2] Institute of Geodesy and Geophysics, Chinese Academy of Sciences, Xudong Street 340, Wuhan 430077, China

[3] Shanxi Administration of Surveying, Mapping and Geoinformation, Yingze Street 136, Taiyuan 030001, China; E-Mail: srl_2014yo@sina.cn

[4] Wanfang College of Science & Technology, Henan Polytechnic University, Qiancheng North Road 8, Vocational Education Park, Zhengzhou 451400, China; E-Mail: wangcaili1983@sina.cn

* Author to whom correspondence should be addressed; E-Mail: lijunming_dr@126.com; Tel.: +86-150-3401-7966.

Abstract: This paper proposes a practical split-window algorithm (SWA) for retrieving land surface temperature (LST) from Landsat-8 Thermal Infrared Sensor (TIRS) data. This SWA has a universal applicability and a set of parameters that can be applied when retrieving LSTs year-round. The atmospheric transmittance and the land surface emissivity (LSE), the essential SWA input parameters, of the Landsat-8 TIRS data are determined in this paper. We also analysed the error sensitivity of these SWA input parameters. The accuracy evaluation of the proposed SWA in this paper was conducted using the software MODTRAN 4.0. The root mean square error (RMSE) of the simulated LST using the mid-latitude summer atmospheric profile is 0.51 K, improving on the result of 0.93 K from Rozenstein (2014). Among the 90 simulated data points, the maximum absolute error is 0.99 °C, and the minimum absolute error is 0.02 °C. Under the Tropical model and 1976 US standard atmospheric conditions, the RMSE of the LST errors are 0.70 K and 0.63 K, respectively. The accuracy results indicate that the SWA provides an LST retrieval method that features not only high accuracy but also a certain universality. Additionally,

the SWA was applied to retrieve the LST of an urban area using two Landsat-8 images. The SWA presented in this paper should promote the application of Landsat-8 data in the study of environmental evolution.

Keywords: Landsat-8; land surface temperature (LST); split-window algorithm (SWA); land surface emissivity (LSE)

1. Introduction

Land surface temperature (LST) plays a significant role in environmental evolution, including heat energy circulation and the water cycle. Retrieving LST from remote sensing data is an important capability for researching the spatial evolution of the regulation of the heat environment at local and global scales [1–4]. Studies on the derivation of LST using satellites have been conducted primarily using NOAA AVHRR data [5,6] at a regional scale. Landsat Thematic Mapper (TM) and Enhanced Thematic Mapper Plus (ETM+) thermal infrared (TIR) data have been used in local-scale studies of LST distributions [7–9]. Data from medium-resolution thermal infrared sensors, such as MODIS and AVHRR with daily temporal resolution, and high-resolution thermal infrared sensors, such as the Landsat series that pass once every 16 days, have been supplied to the public in recent decades [10]. Many studies on the retrieval of LSTs from satellite TIR data have been performed since the 1990s. The methods used can be broadly classified into three categories: single-channel methods, multi-channel methods, and multi-angle methods [11]. The single-channel method, also called the mono-window algorithm, utilizes the radiance measured by a sensor in a single channel to retrieve LST using the general radiance transfer equation [12–14]. The multi-channel method, also called the split-window algorithm (SWA), uses the different absorptions of two TIR channels, linearizing or nonlinearizing the radiance transfer equation with respect to the temperature or wavelength. Many efforts have been made to extend the SWA because these algorithms assume that the land surface emissivity (LSE) values in both TIR channels are known [15–27]. The multi-angle method is in accordance with different atmospheric absorptions because of the differential path-lengths associated with observing the same object from various viewing angles [21,24,28–32]. The launch of the Landsat-8 satellite on February 11, 2013 adds to the remote sensing data of the Landsat family, TM and ETM+. The Landsat-8 satellite carries the Operational Land Imager (OLI) with nine bands and Thermal Infrared Sensor (TIRS) with band10 and band11. Using an SWA, the TIRS band10 and band11 provide the atmospheric rectification for the thermal infrared data [33,34]. Jimenez-Munoz and Sobrino *et al.* [35], Rozenstein *et al.* [10] and Du *et al.* [36] proposed three different SWAs for LST retrieval from Landsat-8 TIR data. The objective of this paper is to provide another SWA for retrieving LSTs from Landsat-8 data. We attempt to improve the convenience and accuracy of the LST retrieval of Landsat-8 TIR data and provide an alternative. Although the idea of the SWA presented in this paper is based on the practical split-window algorithm proposed by Mao *et al.* [27], we did not merely transplant Mao's principle; we also studied the input parameter determination and algorithm structures. We conclude that the SWA idea proposed in this study can be not only applied to Landsat-8 TIR data but can also be used with other kinds of remotely sensed thermal infrared data, such as ASTER and MODIS.

In this paper, we have developed a practical SWA for Landsat-8 TIRS data from another perspective and subjected it to a sensitivity analysis and accuracy assessment. Additionally, a specific calculated case for an urban area in China is provided. Specifically, this paper will (1) describe the SWA model and derive the LST calculation; (2) determine the atmospheric transmittance and the emissivity of the ground for the Landsat-8 TIRS; (3) analyse the sensitivity of the essential input parameters and assess the accuracy via simulated data using MODTRAN 4.0; and (4) retrieve the LST of an urban area in China.

2. The SWA for Landsat-8 TIRS

2.1. Theoretical Derivation of the SWA

The theoretical basis of the LST retrieval algorithm is Planck's law, which is based on the thermal radiance of the ground and the heat transfer from the ground through the atmosphere to the remote sensor [27]. According to Planck's law, the thermal emittance from an object can be expressed as Planck's radiance function [37], as follows in Equation (1):

$$B_n(T) = \frac{2hc^2 n^3}{e^{\frac{hcn}{kT}} - 1}$$ (1)

where $B_n(T)$ denotes the object's spectral radiance, T its absolute temperature, k the Boltzmann constant, h the Planck constant, and c the speed of light. The units of $B_n(T)$ are Wm^{-2}sr^{-1}μm^{-1}. The general radiance transfer equation [38] for the remote sensing of LST can be formulated as follows in Equation (2):

$$B_i(T_i) = \varepsilon_i \tau_i B_i(T_s) + \tau_i(1-\varepsilon_i)I_i \downarrow + I_i \uparrow$$ (2)

where T_s is the LST, T_i is the brightness temperature in channel i, ε_i is the ground emissivity and τ_i is the atmospheric transmittance in band i. $B_i(T_s)$ is the ground radiance, and $I_i \downarrow$ and $I_i \uparrow$ are the downward and upward path radiances, respectively. $I_i \downarrow$ and $I_i \uparrow$ can be expressed by Equations (3) and (4), respectively [27]:

$$I_i \downarrow = (1-\tau_i)B_i(T_a^{\downarrow})$$ (3)

$$I_i \uparrow = (1-\tau_i)B_i(T_a)$$ (4)

where $T_a^{\downarrow}$ is the average temperature of the downward radiance of the atmosphere, and T_a is the average temperature of the upward radiance of atmosphere. Every term of the radiance transfer equation includes the Planck function. According to Qin's [39] analysis, few differences result from using T_a instead of $T_a^{\downarrow}$. Therefore, Equation (2) can be written as follows:

$$B_i(T_i) = \varepsilon_i \tau_i B_i(T_s) + \tau_i(1-\varepsilon_i)(1-\tau_i)B_i(T_a) + (1-\tau_i)B_i(T_a)$$ (5)

which can be consolidated as follows:

$$B_i(T_i) = \varepsilon_i \tau_i B_i(T_s) + (1-\tau_i)(1+(1-\varepsilon_i)\tau_i)B_i(T_a)$$ (6)

In Equation (6), the value of $B_i(T_i)$ can be calculated by substituting the brightness temperature T_i into the Planck function. The terms $B_i(T_s)$ and $B_i(T_a)$ need to be simplified. In this paper, considering

the scope of the application and the desired retrieval accuracy, we applied different simplified fitting methods for $B_i(T_s)$ and $B_i(T_a)$. Because $B_i(T_s)$ has a greater impact on the retrieval precision and it contains inversion parameters, we decided to nonlinearly fit it with a quadratic function, whereas $B_i(T_a)$, which has less impact on the retrieval accuracy, can be linearly fit. Then, Equation (6) can be written as follows:

$$\varepsilon_i \tau_i (a_i T_s^2 + b_i T_s + c_i) + (1-\tau_i)(1+(1-\varepsilon_i)\tau_i)(k_i T_a + d_i) - B_i(T_i) = 0 \tag{7}$$

If the equation is condensed by setting

$$\begin{cases} A_i = \varepsilon_i \tau_i a_i \\ B_i = \varepsilon_i \tau_i b_i \\ C_i = (1-\tau_i)(1+(1-\varepsilon_i)\tau_i)k_i \\ D_i = \varepsilon_i \tau_i c_i + (1-\tau_i)(1+(1-\varepsilon_i)\tau_i)d_i - B_i(T_i) \\ B_i(T_i) = 2hc^2 n^3 / (e^{\frac{hcn_i}{kT_i}} - 1) \end{cases}$$

Then, Equation (7) can be expressed as follows:

$$A_i T_s^2 + B_i T_s + C_i T_a + D_i = 0 \tag{8}$$

For Landsat-8 TIRS band10 and band11, Equation (8) generates the following equation set:

$$\begin{cases} A_{10} T_s^2 + B_{10} T_s + C_{10} T_a + D_{10} = 0 \\ A_{11} T_s^2 + B_{11} T_s + C_{11} T_a + D_{11} = 0 \end{cases} \tag{9}$$

or, upon consolidation,

$$(C_{11}A_{10} - C_{10}A_{11})T_s^2 + (C_{11}B_{10} - C_{10}B_{11})T_s + (C_{11}D_{10} - C_{10}D_{11}) = 0 \tag{10}$$

When this equation is solved for T_s, the result can be expressed as

$$T_s = [(C_{10}B_{11} - C_{11}B_{10}) + \sqrt{(C_{10}B_{11} - C_{11}B_{10})^2 - 4(C_{11}A_{10} - C_{10}A_{11})(C_{11}D_{10} - C_{10}D_{11})}] / [2(C_{11}A_{10} - C_{10}A_{11})] \tag{11}$$

which can be generalized to:

$$(T_s + \xi)^2 = [\alpha B_{10}(T_{10}) - \beta B_{11}(T_{11})] + \psi \tag{12}$$
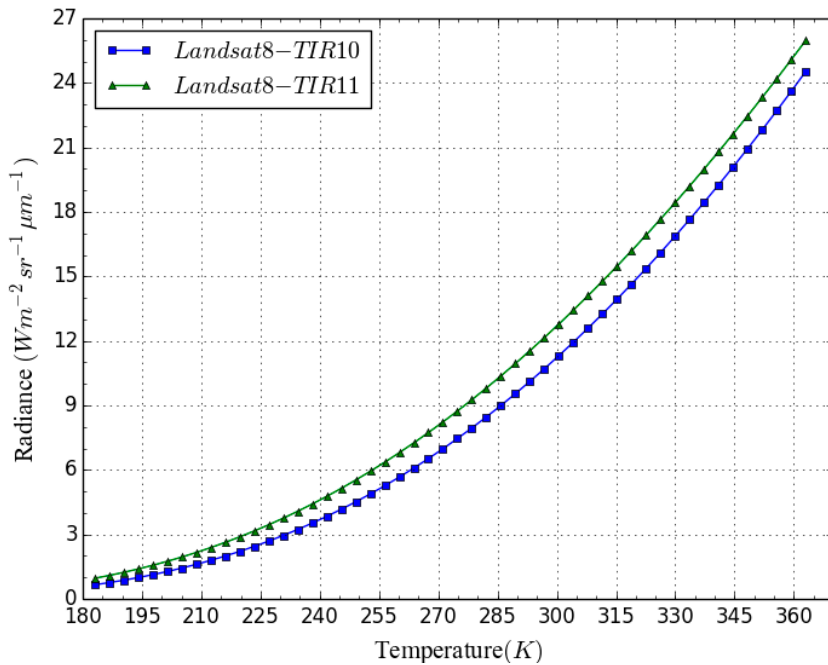
where $\xi, \alpha, \beta,$ and ψ are parameters computed by $\tau_{10}, \varepsilon_{10}, \tau_{11},$ and ε_{11}, respectively.

2.2. Determination of Coefficients

2.2.1. Determination of the Fitting Parameters for $B_i(T_s)$ and $B_i(T_a)$

This study simplified $B_i(T_s)$ via a quadratic fitting method and $B_i(T_a)$ via a linear simplification approach. To strengthen the universality of the model, the temperature range is set from 180 K–363 K (−90 °C–90 °C) for Landsat-8 thermal infrared bands 10 and 11. The selection of the temperature range is based on a full consideration of the existence of extreme surface temperature regions. The extreme minimum temperature was reported to have reached −71 °C in Oymyakon village in Russia, and the surface temperature reached as high as 82.3 °C in several desert areas in the summer. Based on the TIR spectral response function of Landsat-8, the effective wavelengths [40] and wavenumbers of these TIRS are calculated to be 10.9034 μm and 917.1417608 cm^{-1} for the minimum temperature, respectively, and 12.0028 μm and 833.1387464 cm^{-1} for the maximum temperature, respectively.

Then, the thermal radiation values can be obtained using Equation (1). The corresponding Planck curve is shown in Figure 1. The quadratic fitting function is shown in Table 1, the linear regression formula is listed in Table 2, and the fitting parameters $B_i(T_s)$ and $B_i(T_a)$ are listed in Table 3.

Figure 1. The Planck radiance-temperature (180 K–363 K) curve of the Landsat-8 TIRS.

Table 1. The quadratic fitting results for the Landsat-8 TIRS.

TIRS	Quadratic Fitting Expression	R^2	SEE
band10	$B_{10}(T_s) = 0.0006678T_s^2 - 0.2333226T_s + 21.1666266$	0.999979	0.0309
band11	$B_{11}(T_s) = 0.0006188T_s^2 - 0.1990475T_s + 16.7224278$	0.999997	0.0117

Table 2. The linear regression results for the Landsat-8 TIRS.

TIRS	Linear Regression Results	R^2	SEE
band10	$B_{10}(T_a) = 0.1312942T_a - 26.7808503$	0.9465	1.6404
band11	$B_{11}(T_a) = 0.1387986T_a - 27.7043284$	0.9584	1.5193

Table 3. The fitting parameters of $B_i(T_s)$ and $B_i(T_a)$ for the Landsat-8 TIRS.

TIRS	Fitting Parameters	
	Quadratic Fitting Parameters $B_i(T_s) = a_i T_s^2 + b_i T_s + c_i$	Linear Regression Parameters $B_i(T_a) = k_i T_a + d_i$
band10	$a_{10} = 0.0006678$ $b_{10} = -0.2333226$ $c_{10} = 21.1666266$	$k_{10} = 0.1312942$ $d_{10} = -26.7808503$
band11	$a_{11} = 0.0006188$ $b_{11} = -0.1990475$ $c_{11} = 16.7224278$	$k_{11} = 0.1387986$ $d_{11} = -27.7043284$

2.2.2. Determination of Atmospheric Transmittance

The atmospheric transmittance is an important factor in the split-window algorithm. According to previous studies, the atmospheric transmittance strongly depends on the atmospheric water vapour

content, especially for thermal bands [27]. This paper studied the relationship between the Landsat-8 TIRS' atmospheric transmittance estimates and the water vapour in the atmosphere via MORTRAN 4.0 simulations that use the Mid-Latitude Summer atmosphere profile. The simulation data are listed in Table 4. Cubic polynomial fits are adopted for the relationship between the atmospheric water vapour content and transmittance, and the fitting expressions are shown in Table 5. The agreement is very satisfactory. Because the errors in the water vapour content are 0.20 g·cm^{-2} [41] and 0.10 g·cm^{-2}, the corresponding atmospheric transmittance evaluation errors are less than 0.031 and 0.016, respectively.

Table 4. The water vapour of the atmosphere and the corresponding atmospheric transmittance as simulated by MORTRAN 4.0.

Water Vapour Content (g·cm^{-2})	TIR10- τ_{10}	TIR11- τ_{11}
0.5	0.93542	0.89660
0.6	0.92903	0.88448
0.7	0.92217	0.87220
0.8	0.91483	0.85967
0.9	0.90700	0.84686
1.0	0.89869	0.83372
1.1	0.88990	0.82021
1.2	0.88064	0.80637
1.3	0.87093	0.79215
1.4	0.86076	0.77758
1.5	0.85015	0.76266
1.6	0.83913	0.74742
1.7	0.82769	0.73187
1.8	0.81588	0.71603
1.9	0.80370	0.69993
2.0	0.79117	0.68360
2.1	0.77830	0.66706
2.2	0.76514	0.65034
2.3	0.75168	0.63347
2.4	0.73798	0.61649
2.5	0.72401	0.59941
2.6	0.70983	0.58229
2.7	0.69546	0.56512
2.8	0.68092	0.54797
2.9	0.66622	0.53084
3.0	0.65140	0.51378

Table 5. The cubic fit regression functions of the atmospheric transmittance and water vapour content range of 0.5–3.0 g·cm^{-2}.

TIRS	Cubic Regression Results	R^2	SEE
band10	$\tau_{10} = 0.9570356 - 0.0277340w - 0.0333734w^2 + 0.0028800w^3$	0.999999	0.0001
band11	$\tau_{11} = 0.9456728 - 0.0857755w - 0.0290912w^2 + 0.0032169w^3$	0.999995	0.0003

The water vapour content *w* was estimated using the same daytime MODIS data. Although the times of MODIS and Landsat-8 cannot be strictly the same, the Terra satellite carrying MODIS transits the study area approximately 43 minutes earlier than Landsat-8 ((approximately 02:35 *versus* approximately 03:08). The study area is ringed by mountains on three sides, and we have therefore assumed that the water vapour content *w* is constant during this time. Kaufmann, Y. J. *et al.* [42] provided a method to compute the water vapour content in the atmosphere using the reflectance of band2 and band19 of MODIS; thus, we can obtain the water vapour content of the atmosphere using Equation (13).

$$w = \left(\frac{\alpha - \ln(r_{19} / r_2)}{\beta} \right)^2 \tag{13}$$

where *w* is the water vapour content in g·cm^{-2}, $\alpha = 0.020$, $\beta = 0.651$, and r_{19} and r_2 denote the reflectance of MODIS band19 and band2, respectively.

2.2.3. Determination of the Emissivity of the Ground

In consideration of the high signal-to-noise ratio (SNR), this study employed the NDVI threshold method, which considers the differing impacts of distinct land cover types (e.g., water, vegetation, bare soil and impervious surfaces), proposed by Sobrino *et al.* [43] to determine the land surface emissivity (LSE).

We have also referred to the ASTER spectral database[44] to determine the emissivity values of water, vegetation and non-vegetation for Landsat-8 TIRS band10 and band11 (Table 6). Water pixels with negative NDVI values (NDVI < 0) were set to LSE values of 0.991 and 0.986 for band10 and band11, respectively. Fully vegetated pixels with a NDVI value greater than 0.50 were set to LSE values of 0.984 and 0.980. Non-water pixels with NDVI less than 0.20 are considered to be non-vegetated areas, and the LSE values of these pixels were set to 0.964 and 0.970. Finally, pixels with NDVI values greater than 0.20 and less than 0.50 are considered to be mixed pixels incorporating various degrees of vegetation and non-vegetation. The LSE values of these pixels were calculated using Equations (14) and (15) [45–47].

$$\varepsilon_{imix} = \varepsilon_{iv} p_v + \varepsilon_{in} (1 - p_v) + (1 - \varepsilon_{in})(1 - p_v) F \varepsilon_{iv} \tag{14}$$

$$p_v = \left(\frac{NDVI - NDVI_{min}}{NDVI_{\max} - NDVI_{min}} \right)^2 \tag{15}$$

where ε_{imix} is the emissivity of the mixed pixels for band10 and band11, ε_{iv} is the emissivity of the fully vegetated pixels for band10 and band11, ε_{in} is the emissivity of the non-water and non-vegetated pixels for band10 and band11, and F = 0.55 is a shape factor considering the geometrical distribution [48]. The parameter p_v is the scaled *NDVI* value, in which *NDVImin* and *NDVImax* are the *NDVI* values for non-vegetated and fully vegetated land covers, respectively. Please note that, in recent years, colourful steel plates mainly composed of electro-galvanized steels have been installed in architectural fields, with blue-coloured plates being especially common. As a result, regions with blue roof plates in our study area are relatively prevalent. Because the corresponding NDVI of these blue colour steels is relatively large, generally above 0.20 and sometimes even as high as 0.53, we separated these areas from the 0.20–0.50 range of NDVI to produce amplitude ratio values. According to the ASTER spectral database, the Roofing Materials--Galvanized Steel Metal category features wavelengths of 10.9009 μm and

12.0108 μm and corresponding reflectances of 0.041 and 0.038. Therefore, we calculated the Galvanized Steel Metal emissivity values in band10 and band11 to be 0.959 and 0.962, respectively.

Table 6. The emissivity values of water, vegetation and non-vegetation for Landsat-8 TIRS band10, and band11.

	ε_{water}	$\varepsilon_{vegetation}$	$\varepsilon_{non\text{-}vegetation}$	$\varepsilon_{Galvanized\text{-}Steel}$
TIR-band10	0.991	0.984	0.964	0.959
TIR-band11	0.986	0.980	0.970	0.962

3. Steadiness Analysis and Validation of the SWA
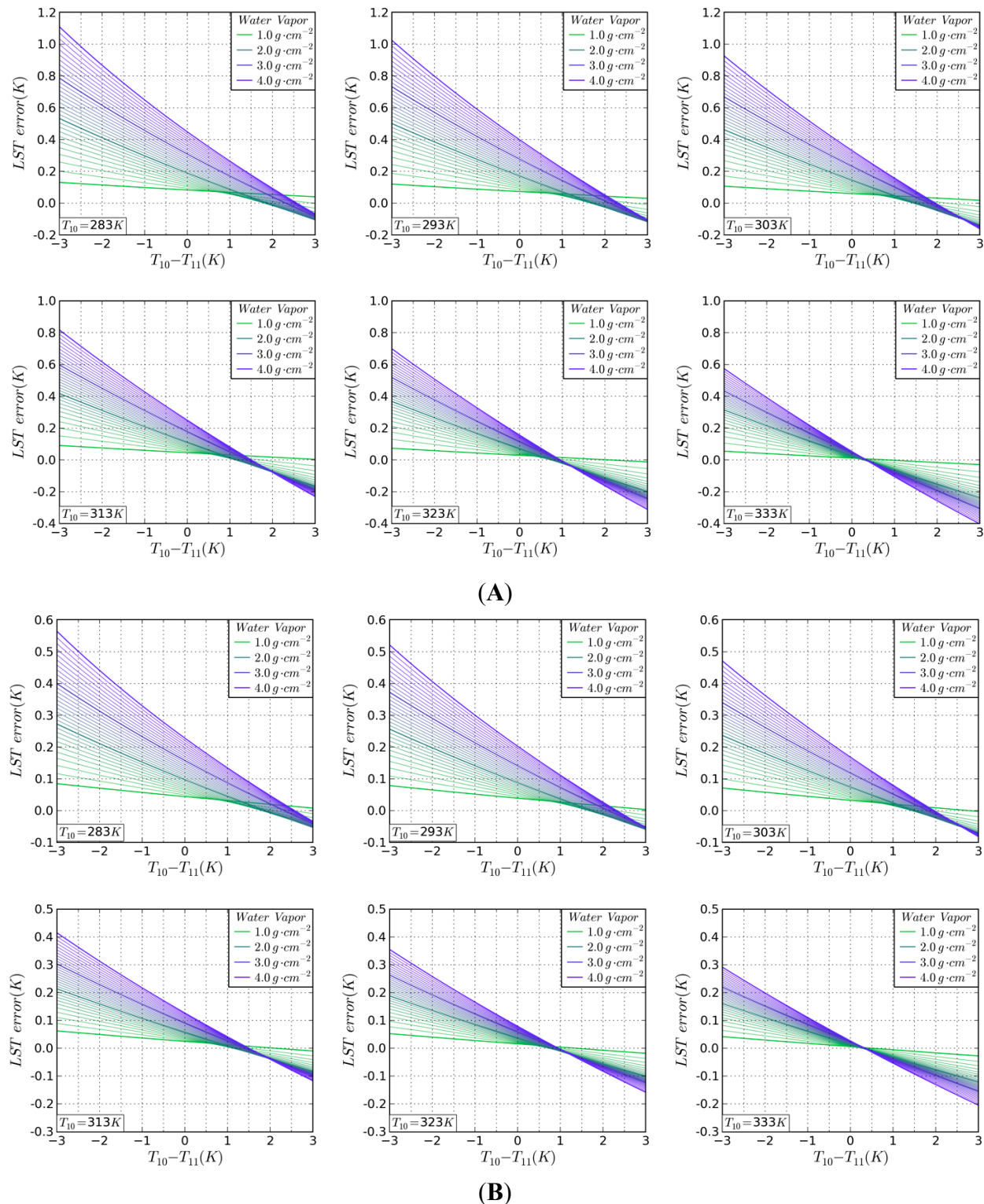
3.1. Steadiness Analysis of the SWA

To assess the steadiness of the SWA proposed in the paper, we analysed the impact of misestimated SWA input parameters on the LST derivation error. The atmospheric transmittance calculated through the atmosphere's water vapour content and the LSE play a major role in the SWA; thus, the influences of these two input parameters were analysed. To enable comparison with the existing SWA proposed by Rozenstein *et al.* (2014), the parameter values were kept almost consistent with that of Rozenstein *et al.* (2014).
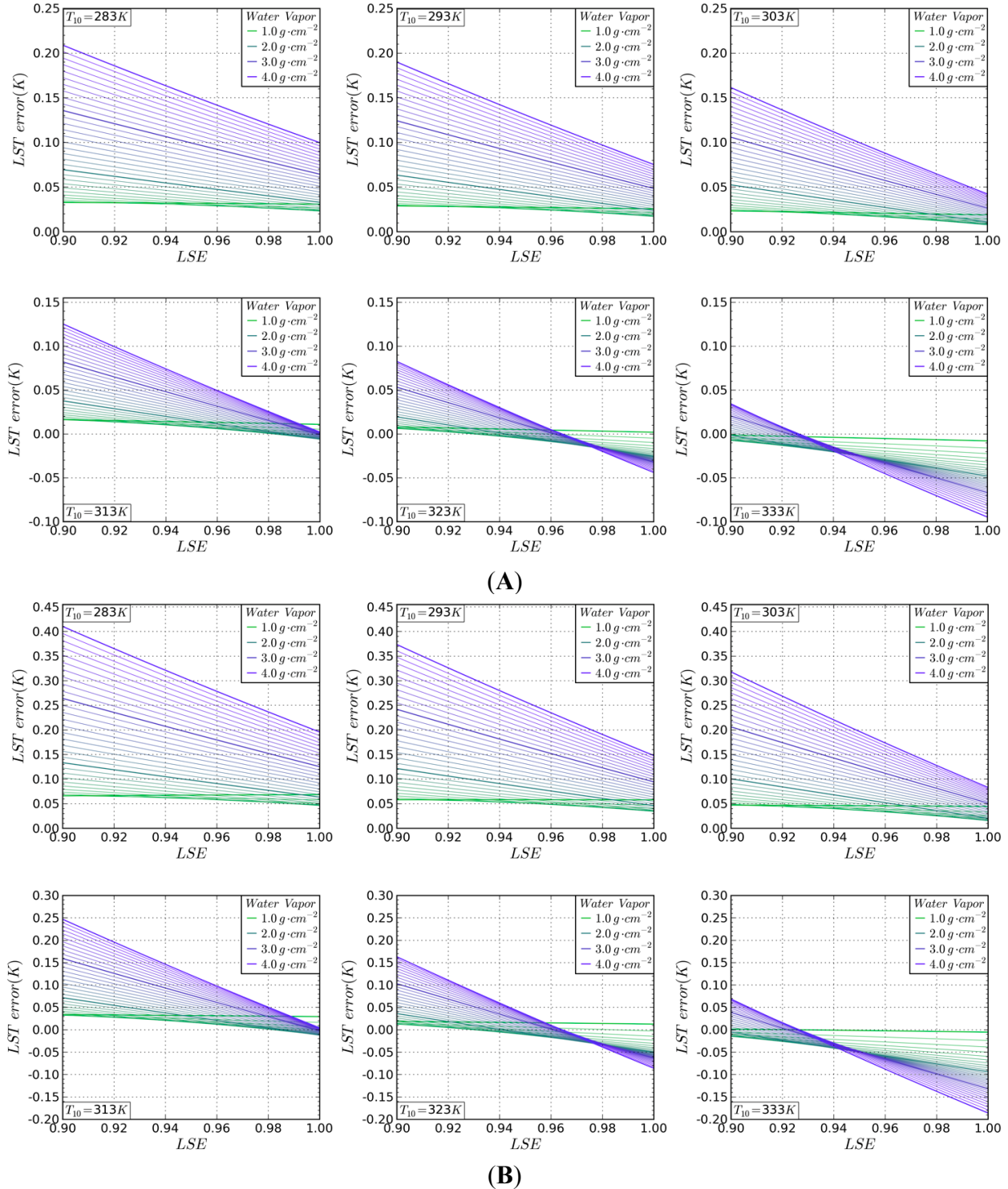
3.1.1. Steadiness Analysis of Atmospheric Transmittance

The atmospheric transmittance is estimated from the water vapour content of the atmosphere. The impact of misestimating the input parameter of the atmosphere transmittance can be assessed by the water vapour content in the column, which is taken to be an important input parameter for the SWA. Because the LST error is related to the brightness temperatures of band10 and band11, we set T_{10} = 283.0–333.0 K, with an interval of 10.0 K, for a T_{10}–T_{11} difference of −3–3 K to calculate the LST estimation error, assuming e_{10} = 0.967 and e_{11} = 0.971 and undervaluing the atmospheric water vapour content by 0.1 and 0.2 g·cm^{-2}, as was done by Rozenstein *et al.* (2014) The water vapour content range was 1.0–4.0 g·cm^{-2}.

The LST estimation error is large when the atmospheric water vapour content is 4.0 g·cm^{-2} and T_{10} is 3 K lower than T_{11}. In addition, for constant values of the other parameters, higher T_{10} values correlate with higher LST errors. The specific error variation is shown in Figure 2A,B. In the case of underestimating the water vapour content by 0.1 g·cm^{-2} and 0.2 g·cm^{-2}, the corresponding maximum LST errors are 0.56 K and 1.11 K, respectively, and the RMSEs of the LST error are 0.30 K and 0.59 K, respectively. The contribution of the calculated atmospheric transmittance error to the retrieved LST is not only related to the water vapour content but also correlates with the LSEs of band10 and band11. The ratio of the LSEs of band10 and band11 is invariant in the analysis process. When the water vapour content column is undervalued by 0.1 and 0.2 g·cm^{-2}, the corresponding maximum LST errors are 0.21 K and 0.41 K, respectively, and the RMSEs of the LST error are 0.10 K and 0.19 K, respectively, as illustrated in Figure 3A,B.

Figure 2. (**A**) The LST evaluated error (K) in the case of undervaluing the atmospheric water vapour content by 0.1 g·cm⁻² for a water vapour content in the range of 1.0–4.0 g·cm⁻² and an interval of 1.0 g·cm⁻² over six gradations of T_{10} = 283.0–333.0 K and a T_{10}–T_{11} value range of −3.0–3.0K. e_{10} = 0.967, and e_{11} = 0.971. (**B**) The LST evaluation error (K) for undervaluing the atmospheric water vapour content by 0.2 g·cm⁻² under the same conditions as in (A).
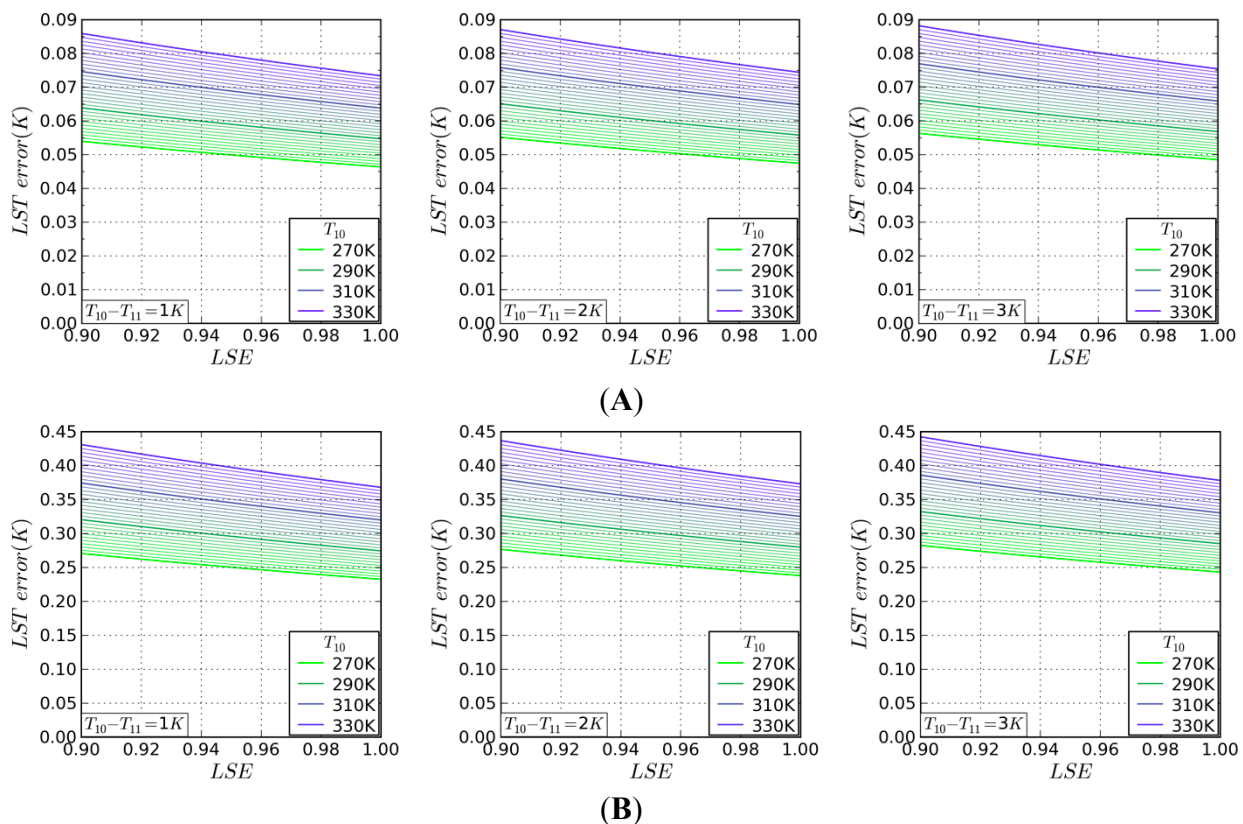
Figure 3. The LST evaluation error (K) in the case of undervaluing the atmospheric water vapour content by 0.1 g·cm^{-2} (**A**) and 0.2 g·cm^{-2} (**B**) for water vapour contents in the range of 1.0–4.0 g·cm^{-2} at an interval of 1.0 g·cm^{-2} over six gradations of T_{10} = 283.0–333.0 K and a T_{10}–T_{11} value of 1 K. The LSE variable is independent.

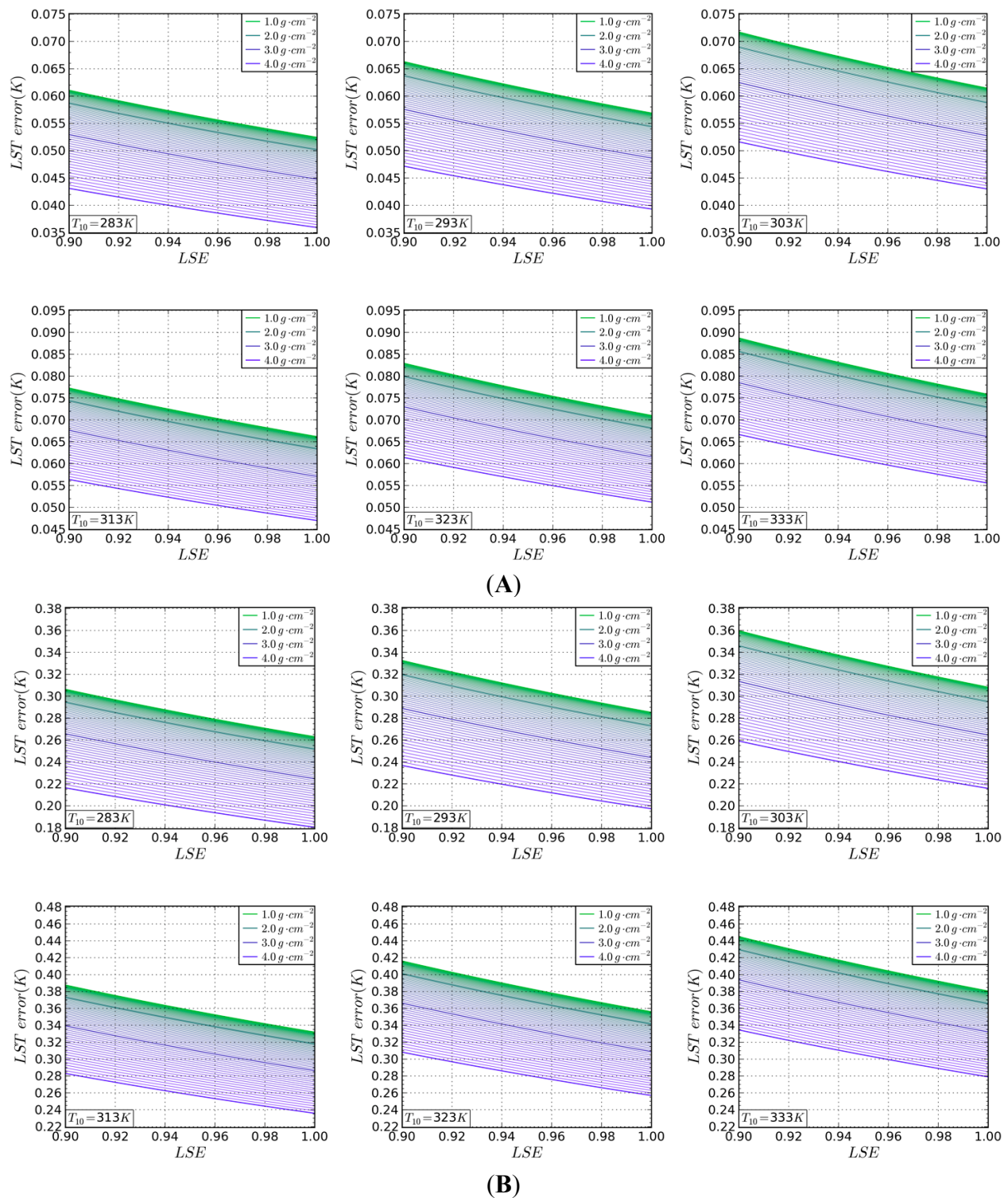3.1.2. Stability Analysis of LSE

Due to the possibility of having separate LSE errors in both bands, the impact on the LST estimation error of simultaneous errors in the LSE values of both band10 and band11 is discussed in

the following. The LSE estimation error also generates an LST calculation error when the atmospheric transmittance has been precisely estimated. In general, the LST calculation error has a positive correlation with the T_{10} and T_{10}–T_{11} values and has a negative correlation with LSE, as illustrated in Figure 4A,B. To be specific, the maximum LST calculation error, 0.44 K, occurs when T_{10} is 330 K, the T_{10}–T_{11} value is 3 K and the LSE is 0.900 due to undervaluing by 0.005. In the case of underestimating the LSE by 0.001, the maximum LST calculation error is 0.09 K. In Figure 4A,B, the atmospheric water vapour content was kept constant at 1.5 g·cm^{-2}. The sensitivity of the LSE to the LST estimation error was analysed as the atmospheric water vapour content varied from 1.0–4.0 g·cm^{-2}, as seen in Figure 5A,B. The LST calculation error has a positive correlation with the T_{10} value and has a negative correlation with LSE and water vapour content. The maximum LST calculation error, 0.45 K, occurs when T_{10} is 333 K, the water vapour content is 1.0 g·cm^{-2}, and LSE is 0.900 due to undervaluing by 0.005.

Generally speaking, the SWA presented in this paper is stable with respect to the impact of incorrectly estimating the LSE and the atmospheric transmittance, *i.e.*, the atmospheric water vapour content. Furthermore, the LST evaluation error is negatively correlated with the LSE estimate.

Figure 4. The illustration of the LST calculation error (K) in the case of undervaluing LSE by 0.001 (**A**) and 0.005 (**B**) over four gradations of T_{10} = 270.0–330.0 K with an interval of 20 K. The atmospheric water vapour content was constant at 1.5 g·cm^{-2}, and the T_{10}–T_{11} values were 1.0, 2.0, and 3.0 K. The LSE variable is independent.

Figure 5. The illustration of the LST calculation error (K) in the case of undervaluing LSE by 0.001 (**A**); and 0.005 (**B**) over six gradations of T_{10} = 283.0–333.0 K with an interval of 10.0 K. The atmospheric water vapour content varies in the range of 1.0–4.0 g·cm^{-2} with an interval of 1.0 g·cm^{-2}, and the T_{10}–T_{11} value is 1.0 K. The LSE variable is independent.

3.2. Evaluation of the Accuracy of the Proposed SWA

MODTRAN 4.0 was used to simulate a series of thermal radiation processes from the ground to the sensor based on the Mid-Latitude Summer atmospheric profile with specified LST, LSE and water vapour content values to evaluate the accuracy of the SWA. First, the simulated thermal radiance values were converted to brightness temperatures corresponding to the Landsat-8 TIRS, band10 and band11, as T_i input parameters for the SWA. Then, according to our SWA and the given input parameters, the LST was calculated. Finally, the LST evaluation errors were obtained by calculating the difference between the given and calculated LSTs. The 90 combination scenes are listed in Table 6. The water vapour content values were 1.0, 2.0, or 3.0 g·cm^{-2}, the range of the assumed LST values was 10–60 °C, with an interval of 10.0 °C, and the range of the LSE values was 0.940–0.980, with an interval of 0.010. The accuracy assessment results, shown in Table 7, are satisfactory, and the RMSE of the LST estimation errors is 0.51 °C, outperforming the result of 0.93 °C from Rozenstein *et al*. (2014). To assess the general applicability of this SWA to different atmospheric conditions, we also evaluated the accuracy of this SWA under a tropical model and 1976 US standard atmospheric conditions. The assessment results are listed in Tables 8 and 9. The RMSEs of the LST errors under the tropical model and the 1976 US standard atmospheric conditions are 0.70 °C and 0.63 °C, respectively.

Table 7. Estimation errors of LST for different simulated combinations of specified LST, LSE, and water vapour content values based on the Mid-Latitude Summer atmospheric profile.

Water Vapour Content (g·cm^{-2})	LST (°C)	LSE = 0.980	LSE = 0.970	LSE = 0.960	LSE = 0.950	LSE = 0.940
1	10	0.3710	0.3641	0.3561	0.3492	0.3413
	20	0.3384	0.3302	0.3220	0.3138	0.3056
	30	0.3993	0.3914	0.3921	0.3691	0.3700
	40	0.5339	0.5348	0.5221	0.5232	0.5103
	50	0.7360	0.7350	0.7268	0.7186	0.7178
	60	0.9933	0.9870	0.9926	0.9864	0.9731
2	10	0.3235	0.2868	0.2550	0.2231	0.1897
	20	0.2835	0.2605	0.2238	0.2007	0.1635
	30	0.3388	0.3250	0.2833	0.2586	0.2450
	40	0.4810	0.4671	0.4374	0.4075	0.3936
	50	0.6935	0.6682	0.6520	0.6264	0.6102
	60	0.9515	0.9278	0.9177	0.8939	0.8611
3	10	0.1532	0.0701	−0.0164	−0.1170	−0.2146
	20	0.1456	0.0527	−0.0281	−0.1099	−0.1927
	30	0.2104	0.1390	0.0603	−0.0194	−0.0933
	40	0.3684	0.2865	0.2227	0.1388	0.0734
	50	0.5708	0.5059	0.4403	0.3739	0.3067
	60	0.8190	0.7716	0.7073	0.6423	0.5933

Table 8. Estimation errors of LST for different simulated combinations of specified LST, LSE, and water vapour content values based on the Tropical model atmospheric profile, RMSE = 0.70 °C.

Water Vapour Content (g·cm⁻²)	LST (°C)	LSE = 0.980	LSE = 0.960	LSE = 0.940
1.0	20	0.3130	0.2958	0.2766
	40	0.5476	0.5326	0.5163
	60	1.0371	1.0250	1.0122
2.0	20	0.3078	0.2415	0.1730
	40	0.5845	0.5282	0.4723
	60	1.1176	1.0713	1.0220
3.0	20	0.2281	0.0416	−0.1486
	40	0.6080	0.4500	0.2914
	60	1.2313	1.0958	0.9587

Table 9. Estimation errors of LST for different simulated combinations of specified LST, LSE, and water vapour content values based on the 1976 US Standard atmospheric profile, RMSE = 0.63 °C.

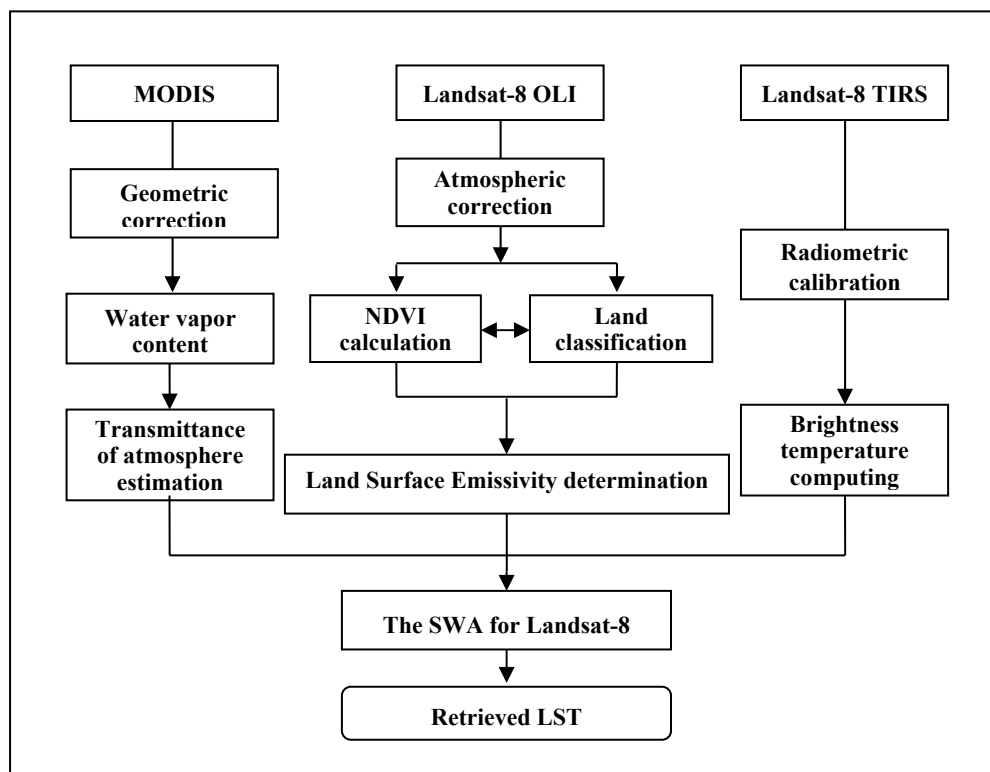| Water Vapour Content (g·cm⁻²)	LST (°C)	LSE = 0.980	LSE = 0.960	LSE = 0.940
1.0	20	0.3893	0.3836	0.3762
	40	0.5563	0.5511	0.5439
	60	0.9996	0.9940	0.9893
2.0	20	0.3129	0.2704	0.2288
	40	0.4576	0.4206	0.3851
	60	0.8739	0.8440	0.8145
3.0	20	0.2749	0.1358	−0.0071
	40	0.5500	0.4310	0.3118
	60	1.0849	0.9823	0.8787

4. A Case Study of an Urban Area in China

4.1. Study Area

The city of Taiyuan-Yuci, China, was chosen as the urban study area. This urban area is located in north-central China, between 37°24'–38°04'N and 112°09'–113°06'E. Taiyuan-Yuci covers a land area of 3336 km² and has approximately 4.41 million inhabitants (China, the data of the Sixth Population Census, 2010). The region features a warm continental monsoon climate.

4.2. Data Used

Two cloud-free Landsat-8 images, acquired at UTC 03:08:38 on June 27, 2013 and UTC 03:06:26 on June 30, 2014, were rectified to a Universal Transverse Mercator (UTM) projection with WGS-84 datum and UTM zone 49. Two daytime MODIS-Terra images acquired at 02:35 and 04:10 on June 27, 2013 and June 30, 2014, respectively, are also used in this paper to calculate the water vapour content
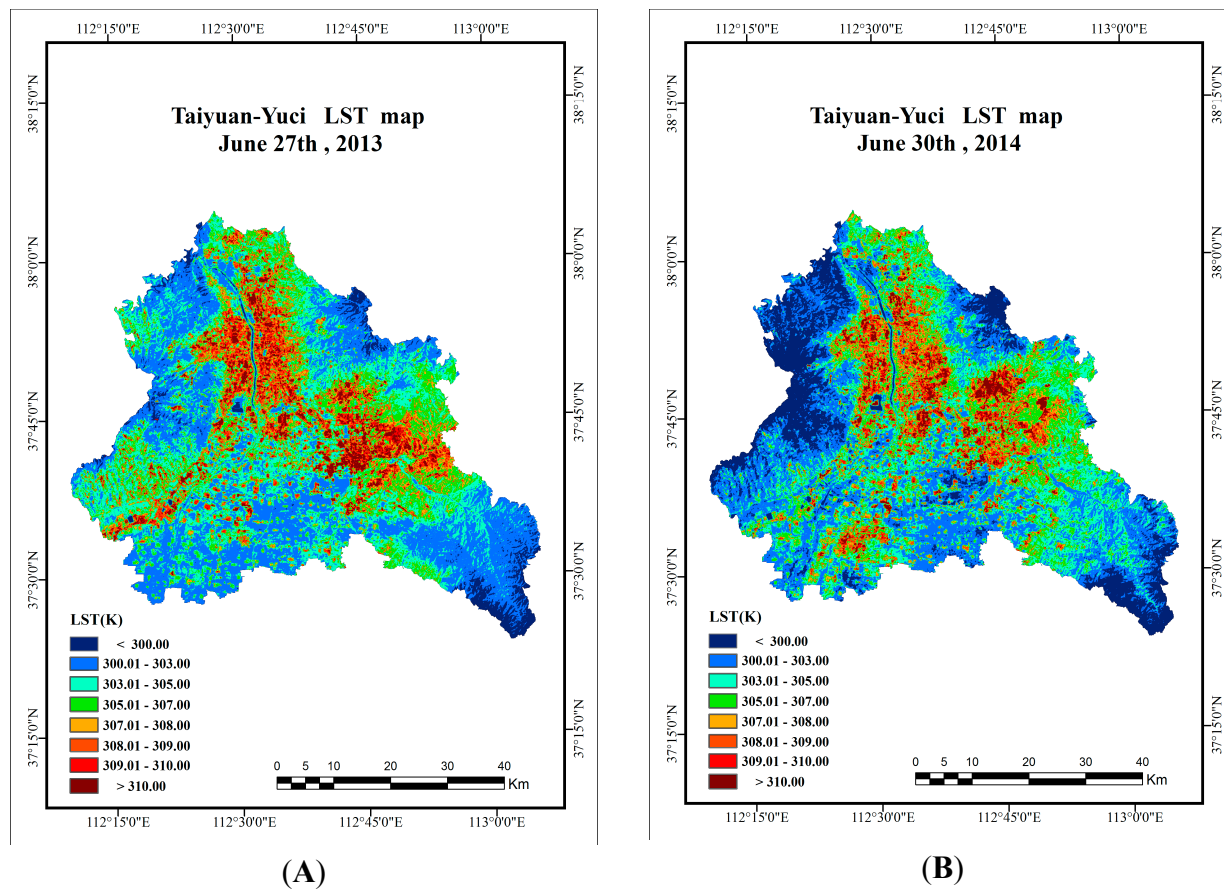
of the atmosphere. Because the MODIS and Landsat-8 acquisition times on the same day were not rigidly consistent, we used the average value of the two temporal MODIS water vapour content estimates to calculate the water vapour content of the atmosphere when the Landsat-8 satellite passed over the study area.

Figure 6. Workflow for retrieving LST from Landsat-8 data.

4.3. LST Retrieval

Using the SWA proposed in this paper, the LST of the urban area was retrieved via the workflow shown in Figure 6. Three sets of input parameters, $B_{10}(T_{10})$ and $B_{11}(T_{11})$, τ_{10} and τ_{11}, and ε_{10} and ε_{11}, need to be calculated. The spectral radiance values, $B_{10}(T_{10})$ and $B_{11}(T_{11})$, can be computed from the brightness temperatures T_{10} and T_{11} using Planck's radiance function. The atmospheric water vapour content images were produced by using the MOD021KM datasets in conjunction with Equation (13). The obtained water vapour images were then resampled to 30 m × 30 m in accordance with the daytime Landsat-8 images. According to the cubic fit functions of the atmospheric transmittance and water vapour content, the atmospheric transmittance values, τ_{10} and τ_{11}, were confirmed. Using Landsat-8 OLI datasets, NDVI images were retrieved. The LSE, ε_{10} and ε_{11} can be confirmed with the NDVI images and Equations (14) and (15), and the emissivity values are listed in Table 6. The three input parameters have now all been confirmed and entered into the SWA formula, and the LST images have been produced. Figure 7 shows the LST estimated from the Landsat-8 TIR data. The LST on June 27, 2013, ranges from 296.6 K–323.8 K, with a mean value of 304.5 K and a standard deviation of 2.953 K. The LST on June 30, 2014, ranges from 292.4 K–322.9 K, with a mean value of 303.7 K and a standard deviation of 3.490 K.

Figure 7. The LST Spatial distribution of the study urban area retrieved from Landsat-8: (**A**) on June 27, 2013, and (**B**) on June 30, 2014.

5. Conclusions

A practical SWA for Landsat-8 TIRS data was proposed in this paper. The analysis of sensitivity shows that the SWA has good stability. In five sensitivity analysis scenarios using the Mid-Latitude Summer atmospheric profile, the minimum LST error is −0.839 K, and the maximum LST error is 0.786 K. In general, the LST error is very sensitive when the water vapour content and T_{10}–T_{11} change together, as is seen in Figure 2B, especially when the water vapour content is 0.5–1.0 g·cm^{-2}. Based on the validation results of the simulation data generated by MODTRAN 4.0, the SWA performs very well. The verification result is satisfactory in that the maximum and minimum LST errors are 0.993 K and 0.016 K, respectively, and the LST error RMSE is 0.51 K under Mid-Latitude Summer atmospheric conditions. The LST error RMSEs under Tropical and 1976 US standard atmospheric conditions are 0.70 K and 0.63 K, respectively. The assessment results demonstrate that the SWA is not only steady and accurate but also universal for different atmospheric conditions.

In this paper, we offer a strategy for evaluating the atmospheric water vapour content using MODIS data and for determining the relationship between the atmospheric transmissivity and water vapour content from Landsat-8 TIRS data using simulation data from MODTRAN 4. An exploratory attempt was performed on a corresponding LSE estimation based on Landsat-8 TIRS data, presented by the LSE of three classic earth surfaces and one new earth surface (galvanized coloured roofs), which further improved the SWA's integrality and practicality. Additionally, a complete application was

performed by retrieving the LST of a study area. The proposed SWA in this paper will contribute to the completion of the inversion algorithm system of LST and will promote the application of remote sensing technology in the research of the thermal environment of the Earth.

Acknowledgements

Author Contributions

All authors contributed significantly to this manuscript. The specific contributions include data collection (Meijun Jin, Junming Li and Caili Wang), data processing (Meijun Jin and Ruilan Shang), conceiving the idea and designing the methodology (Junming Li and Meijun Jin), and manuscript writing (Meijun Jin, Junming Li and Caili Wang).

Conflicts of Interest

The authors declare no conflict of interest.

References and Notes

1. Chapin, F.; Sturm, M.; Serreze, M.; McFadden, J.; Key, J.; Lloyd, A.; McGuire, A.; Rupp, T.; Lynch, A.; Schimel, J. Role of Land-Surface Changes in Arctic Summer Warming. *Science* **2005**, *310*, 657–660.
2. Kalnay, E.; Cai, M. Impact of urbanization and land-use change on climate. *Nature* **2003**, *423*, 528–531.
3. Ramanathan, V.; Crutzen, P.; Kiehl, J.; Rosenfeld, D. Aerosols, climate, and the hydrological cycle. *Science* **2001**, *294*, 2119–2124.
4. Wan, Z.; Wang, P.; Li, X. Using MODIS land surface temperature and normalized difference vegetation index products for monitoring drought in the Southern Great Plains, USA. *Int. J. Remote Sens*. **2004**, *25*, 61–72.
5. Gallo, K.P.; Owen, T.W. Assessment of urban heat island: A multi-sensor perspective for the Dallas-Ft. Worth, USA region. *Geocarto. Int.* **1998**, *13*, 35–41.
6. Streutker, D.R. A remote sensing study of the urban heat island of Houston, Texas. *Int. J. Remote Sens.* **2002**, *23*, 2595–2608.
7. Weng, Q. A Remote sensing-GIS evaluation of urban expansion and its impact on surface temperature in the Zhujiang Delta, China. *Int. J. Remote Sens*. **2001**, *22*, 1999–2014.
8. Chen, X.L.; Zhao, H.; Li, P.; Yin, Z. Remote sensing image-based analysis of the relationship between urban heat island and land use/cover changes. *Remote Sens*. *Environ.* **2002**, *104*, 133–146.

9. Yuan, F.; Bauer, M.E. Comparison of impervious surface area and Normalized Difference Vegetation Index as indicators of surface urban heat island effects in Landsat imagery. *Remote Sens. Environ.* **2007**, *106*, 375–386.

10. Rozenstein, O.; Qin, Z.; Derimian, Y.; Karnieli, A. Derivation of land surface temperature for Landsat-8 TIRS using a split window algorithm. *Sensors* **2014**, *14*, 5768–5780.

11. Li, Z.L.; Tang, B.H.; Wu, H.; Ren, H.; Yan, G.; Wan, Z.; Trigo, I.F.; Sobrino, J.A. Satellite-derived land surface temperature: Current status and perspectives. *Remote Sens. Environ.* **2013**, *131*, 14–37.

12. Li, Z.L.; Zhang, R.; Sun, X.; Su, H.; Tang, X.; Zhu, Z. Experimental system for the study of the directional thermal emission of natural surfaces. *Int. J. Remote Sens.* **2004**, *25*, 195–204.

13. Ottlé, C.; Vidal-Madjar, D. Estimation of land surface temperature with NOAA9 data. *Remote Sens. Environ.* **1992**, *40*, 27–41.

14. Price, J.C. Estimating surface temperatures from satellite thermal infrared data—A simple formulation for the atmospheric effect. *Remote Sens. Environ.* **1983**, *13*, 353–361.

15. Price, J.C. Land surface temperature measurements from the split window channels of the NOAA 7 AVHRR. *J. Geophys. Res.* **1984**, *89*, 7231–7237.

16. Becker, F. The impact of spectral emissivity on the measurement of land surface temperature from a satellite. *Int. J. Remote Sens.* **1987**, *8*, 1509–1522.

17. Becker, F.; Li, Z.L. Towards a local split window method over land surfaces. *Int. J. Remote Sens.* **1990**, *11*, 369–393.

18. Sobrino, J.A.; Coll, C.; Caselles, V. Atmospheric correction for land surface temperature using NOAA-11 AVHRR Channels 4 and 5. *Remote Sens. Environ.* **1991**, *38*, 19–34.

19. Coll, C.; Caselles, V.; Sobrino, J.A.; Valor, E. On the atmospheric dependence of the split-window equation for land surface temperature. *Int. J. Remote Sens.* **1994**, *15*, 105–122.

20. Sobrino, J.A.; Li, Z.L.; Stoll, M.P.; Becker, F. Improvements in the split-window technique for land surface temperature determination. *IEEE Trans. Geosci. Remote Sens.* **1994**, *32*, 243–253.

21. Prata, A.J. Land surface temperature determination from satellites. *Adv. Space Res.* **1994**, *14*, 15–26.

22. Ulivieri, C.; Castronuovo, M.M.; Francioni, R.; Cardillo, A. A split window algorithm for estimating land surface temperature from satellites. *Adv. Space Res.* **1994**, *14*, 59–65.

23. Wan, Z.; Dozier, J. A generalized split-window algorithm for retrieving land-surface temperature from space. *IEEE Geosci. Remote Sens.* **1996**, *34*, 892–905.

24. Sobrino, J.A.; Li, Z.L.; Stoll, M.P.; Becker, F. Multi-channel and multi-angle algorithms for estimating sea and land surface temperature with ATSR data. *Int. J. Remote Sens.* **1996**, *17*, 2089–2114.

25. Tang, B.H.; Li, Z.L. Retrieval of land surface bidirectional reflectivity in the mid-infrared from MODIS Channels 22 and 23. *Int. J. Remote Sens.* **2008**, *29*, 4907–4925.

26. Atitar, M.; Sobrino, J.A. A split-window algorithm for estimating LST from Meteosat 9 Data: Test and comparison with *in situ* data and MODIS LSTs. *IEEE Geosci. Remote Sens.* **2009**, *6*, 122–126.

27. Mao, K.; Qin, Z.; Shi, J.; Gong, P. A practical split-window algorithm for retrieving land-surface temperature from MODIS data. *Int. J. Remote Sens.* **2005**, *26*, 3181–3204.

28. Chédin, A.; Scott, N.A.; Berroir, A. A single-channel, double-viewing angle method for sea surface temperature determination from coincident Meteosat and TIROS-N radiometric measurements. *J. Appl. Meteorol.* **1982**, *21*, 613–618.

29. Prata, A.J. Surface temperatures derived from the Advanced Very High Resolution Radiometer and the Along Track Scanning Radiometer. 1. Theory. *J. Geophys. Res*. **1993**, *98*, 16689–16702.

30. Prata, A.J. Land surface temperatures derived from the Advanced Very High Resolution Radiometer and the Along-Track Scanning Radiometer 2. Experimental results and validation of AVHRR algorithms. *J. Geophys. Res*. **1994**, *99*, 13025–13058.

31. Li, Z.L.; Stoll, M.P.; Zhang, R.H.; Jia, L.; Su, Z.B. On the separate retrieval of soil and vegetation temperatures from ATSR data. *Sci. China Series D: Earth Sci.* **2001**, *44*, 97–111.

32. Sobrino, J.A.; Romaguera, M. Land surface temperature retrieval from MSG1-SEVIRI data. *Remote Sens. Environ.* **2004**, *92*, 247–254.

33. Irons, J.R.; Dwyer, J.L.; Barsi, J.A. The next Landsat satellite: The Landsat Data Continuity Mission. *Remote Sens. Environ*. **2012**, *122*, 11–21.

34. Cuenca, R.H.; Ciotti, S.P.; Hagimoto, Y. Application of Landsat to evaluate effects of irrigation forbearance. *Remote Sens*. **2013**, *5*, 3776–3802.

35. Jimenez-Munoz; J.C.; Sobrino; J.A.; Skokovic, D.; Matter, C.; Cristobal, J. Land surface temperature retrieval methods from Landsat-8 Thermal Infrared Sensor data. *IEEE Geosci. Remote Sens*. **2014**, *11*, 1840–1843.

36. Du, C.; Ren, H.Z.; Qin, Q.M.; Meng, J.J.; Li, J. Split-window algorithm For estimating land surface temperature from Landsat 8 TIRs data. In Proceedings of 2014 IEEE International Geoscience and Remote Sensing Symposium (IGARSS), Quebec City, QC, Canada, 13–18 July 2014; pp. 3578–3581.

37. Rybicki, G.B.; Lightman, A.P. *Fundamental of Radiative Transfer. Radiative Processes in Astrophysics*; John Wiley & Sons, Inc.: New York, NY, USA, 1979.

38. Ottle, C.; Stoll, M. Effect of atmospheric absorption and surface emissivity on the determination of land surface temperature from infrared satellite data. *Int. J. Remote Sens*. **1993**, *14*, 2025–2037.

39. Qin, Z.; Karnieli, A. A Mono-Window Algorithm for Retrieving Land Surface Temperature from Landsat TM Data and Its Application to the Israel-Egypt Border Region. *Int. J. Remote Sens*. **2001**, *22*, 3722–3723.

40. Jiménez-Muĺoz, J.C.; Sobrino, J.A. A generalized single 2 channel method for retrieving land surface temperature from remote sensing Data. *J. Geophys. Res*. **2003**, *8*, doi:10.1029/2003JD003480.

41. Qin, Z.; Dall'Olmo, G.; Karnieli, A.; Berliner, P. Derivation of split window algorithm and its sensitivity analysis for retrieving land surface temperature from NOAA-Advanced very High Resolution Radiometer data. *Geophys. Res. Atmos*. **2001**, *106*, 22655–22670.

42. Kaufmann, Y.J.; Gao, B.C. Remote sensing of water in the Near IR from EOS/MODIS. *IEEE Trans. Geosci. Remote Sens*. **1992**, *30*, 871–884.

43. Sobrino, J.A.; Raissouni, N.; Li, Z.L. A comparative study of land surface emissivity retrieval from NOAA data. *Remote Sens. Environ*. **2001**, *75*, 256–266.

44. Aster Spectral Library. Available online: http://speclib.jpl.nasa.gov/ (accessed on 4 June 2014).

45. Carlson, T.N.; Ripley, D.A. On the relation between NDVI, fractional vegetation cover, and leaf area index. *Remote Sens*. *Environ*. **1997**, *62*, 241–252.

46. Sobrino, J.A.; Jiménez-Muñoz, J.C.; Paolini, L. Land surface temperature retrieval from LANDSAT TM 5. *Remote Sens. Environ.* **2004**, *90*, 434–440.

47. Sobrino, J.A.; Raissouni, N. Toward remote sensing methods for land cover dynamic monitoring: Application to Morocco. *Int. J. Remote Sens.* **2000**, *21*, 353–366.

48. Sobrino, J.A.; Caselles, V.; Becker, F. Significance of the remotely sensed thermal infrared measurements obtained over a citrus orchard. *Photogramm. Eng. Remote Sens.* **1990**, *44*, 343–354.